Applied Catalysis B: Environmental 147 (2014) 554–561

Contents lists available at ScienceDirect

Applied Catalysis B: Environmental

journal homepage: www.elsevier.com/locate/apcatb

Significantly enhancement of photocatalytic performances via core–shell structure of ZnO@mpg-C_3N_4

Daimei Chen[a,*], Kewei Wang[a,b,c], Dugao Xiang[a], Ruilong Zong[b], Wenqing Yao[b], Yongfa Zhu[b,*]

[a] National Laboratory of Mineral Materials, School of Materials Sciences and Technology, China University of Geosciences, Beijing 100083, China
[b] Department of Chemistry, Tsinghua University, Beijing, 100084, China
[c] School of Chemical Engineering, Hebei University of Technology, Tianjin 300130, China

ARTICLE INFO

Article history:
Received 5 July 2013
Received in revised form 4 September 2013
Accepted 22 September 2013
Available online 29 September 2013

Keywords:
Photocatalysis
mpg-C_3N_4
ZnO
Core–shell structure

ABSTRACT

ZnO@mpg-C_3N_4 photocatalysts with core–shell structure were synthesized via a facile ultrasonic dispersion method. The thickness of the shell can be adjusted by tuning the amount of mpg-C_3N_4, which is closely connected with the photocatalytic activity. The ZnO@mpg-C_3N_4 sample at a weight ration of 4% (mpg-C_3N_4/ZnO) has the highest UV light photocatalytic activity which is almost 2.0 times as high as that of pure ZnO. While the visible light photocatalytic activity of ZnO@mpg-C_3N_4 increases with the increase of the loading amount of mpg-C_3N_4. The enhanced UV photocatalytic activity of the ZnO@mpg-C_3N_4 photocatalysts could be attributed to the hybridized effect between ZnO and mpg-C_3N_4. The photogenerated holes on ZnO could easily transfer to mpg-C_3N_4, making charge separation more efficient and reducing the probability of recombination. The enhancement of the visible light photocatalytic activity is due to the heterojunction interfaces and the core–shell structure induced by the match of lattice and energy level between the C_3N_4 shell and ZnO core. The C_3N_4 shell absorbs the visible light, and then generates the excited-state electrons. The excited electron on C_3N_4 could directly inject into the CB of ZnO, making ZnO@mpg-C_3N_4 present remarkable visible light photocatalytic activity.

1. Introduction

Photocatalytic degradation of organic pollutants by using nanostructured semiconductors offers great potential for the complete elimination of toxic chemicals. To date, a large number of semiconductor materials like metal oxides and sulfides (such as TiO_2, WO_3, CdS, ZnS, ZnO) have been identified as active photocatalysts for photodegradation of organic pollutants [1–5]. Among them, ZnO is a promising photocatalyst because of its high activity, chemical stability, non-toxicity, abundant availability, low cost and so on [6,7]. However, the high recombination ratio of photoinduced electron–hole pairs and very poor response to visible light and the photocorrosion have hindered the application of ZnO in photocatalysis. Therefore, a plenty of methods such as such as ion doping [8,9], noble metal loading [10,11], or combining ZnO with another semiconductor [12,13], have been applied to enhance the charge separation and improve the visible light response of ZnO based photocatalysts.

In recent years, ZnO hybridized with a conjugative π structure material has been proved to be effective way for enhancing photocatalytic activity. For example, ZnO hybridized with C_{60} [14], polyaniline (PANI) [15] and graphite-like carbon (e.g., C_3N_4) [16] all presents higher photocatalytic activity than the pristine. These π-conjugated materials have also been regarded to increase separation efficiency of photogenerated electron–hole pairs through the formation of electronic interactions with photocatalysts during the catalytic reaction. The graphite-like carbon nitride (g-C_3N_4), as one of the π-conjugated materials, has recently been reported to exhibit a good photocatalytic activity for hydrogen production and organic degradation under visible light irradiation [17,18]. Different from the inorganic π-conjugated materials (e.g., graphite and C_{60}), g-C_3N_4 is a soft polymer so that it can easily coat on other compounds' surface, promoting the formation of core–shell structures. Zhu et al. has successfully prepared the C_3N_4/$BiPO_4$ [19], and C_3N_4/Bi_2WO_6 [20] core–shell structures and found that the photocatalytic activities of these composite photocatalysts were greatly enhanced, which may be not only due to the heterojunction interfaces, but also due to the core–shell structure induced by the lattice match. However, C_3N_4 synthesized by self condensation of organic precursors is bulk material with a big sheet of lamellar structure and a very small surface area, normally below 10 $m^2\ g^{-1}$. This fact makes it difficult to homogenously wrap around the photocatalysts

* Corresponding authors. Tel.: +86 10 82332274; fax: +86 10 82322974.
E-mail addresses: chendaimei@cugb.edu.cn, chendaimei0611.student@sina.com (D. Chen), zhuyf@tsinghua.edu.cn (Y. Zhu).

0926-3373/$ – see front matter © 2013 Elsevier B.V. All rights reserved.
http://dx.doi.org/10.1016/j.apcatb.2013.09.039

and cannot provide more possible reaction sites for the catalytic reaction due to its small surface area.

Mesoporous g-C_3N_4 (mpg-C_3N_4) feathers unique semiconductor properties along with an open crystalline pore wall and a large surface area facilitating mass transfer. The structure can in principle enhance the light harvesting ability and the reactant adsorption capability of the material due to its large surface and multiple scattering effects. In addition, due to many pores on the sheet of C_3N_4, it becomes easier to coat on the other catalyst's surface than bulk C_3N_4. Therefore, in our work, mpg-C_3N_4 was used as a conjugative π structure material to prepare the ZnO@mpg-C_3N_4 core–shell structure material. To the best of our knowledge, this is the first report on ZnO@mpg-C_3N_4 core–shell structure material. The structure of this core–shell structure material and the possible mechanisms of the enhancement of photocatalytic activity were systematically investigated.

2. Experimental

2.1. Material

Cyanamide ($CN–NH_2$) was purchased from Rugao City Zhongru Chemical Co., Ltd, P. R. China. ZnO (particle diameter 30–50 nm, surface area 9.654 $m^2\,g^{-1}$) was obtained from Nanjing Haitai Nanometer Materials Corp, P. R. China. 40% dispersion of SiO_2 particles (particle diameter 12 nm) was supplied by Beijing BOYU GOKE New Material Technology Co., Ltd, PR China. All other reagents used in this research were analytically pure and used without further purification.

2.2. Sample preparation

2.2.1. Synthesis of mpg-C_3N_4

The mpg-C_3N_4 was synthesized with the hard template method as previously reported [21]. An amount of 9.0 g molten cyanamide was added dropwise in 22.5 g of a 40% dispersion of 12-nm SiO_2 particles, which were used as a hard template. The mixture was heated at 90 °C with stirring to evaporate water. The resultant white powder was then heated at a rate of 2.3 °C min^{-1} over 4 h to reach a temperature of 550 °C, and then tempered at this temperature for an additional 4 h. The brown–yellow product was treated with ammonium bifluoride (NH_4HF_2, 4 M) for 48 h to remove the silica template. The powders were then centrifuged and washed with distilled water for four times and with ethanol twice. Finally the mpg-C_3N_4 was dried at 70 °C under vacuum for overnight. The bulk g-C_3N_4 was synthesized by directly heating 9 g of cyanamide at a rate of 2.3 °C min^{-1} over 4 h to reach a temperature of 550 °C, and then tempered at this temperature for an additional 4 h.

2.2.2. Synthesis of core–shell structured ZnO@mpg-C_3N_4 photocatalyst

ZnO@mpg-C_3N_4 was prepared as follows. Firstly, an appropriate amount of mpg-C_3N_4 was added into methanol then the beaker was placed in an ultrasonic bath for 30 min to completely disperse the mpg-C_3N_4. The ZnO powder was added into the above solution and stirred in a fume hood for 24 h. After volatilization of the methanol, an opaque powder was obtained after drying at 100 °C. A series of ZnO@mpg-C_3N_4 photocatalysts with the different mass ratios of ZnO@mpg-C_3N_4 were prepared by this method, which denoted as ZnO@mpg-C_3N_4-X (X = 1%, 2%, 3%, 4%, 5%, 7%, 9%, 11%, 13%, 15%, 20%). For comparison, ZnO@g-C_3N_4 was also prepared using the same method as ZnO@mpg-C_3N_4 photocatalyst.

2.3. Characterization

X-ray diffraction (XRD) patterns of the powders were recorded at room temperature by a Bruker D8 Advance X-ray diffractometer. Morphologies and structures of the prepared samples were further examined with a HITACHI HT770 transmission electron microscopy (TEM) operated at an accelerating voltage of 100 kV. High-resolution transmission electron microscopy (HRTEM) images were obtained by a JEOL JEM-2011F field emission transmission electron microscope with an accelerating voltage of 200 kV. Fourier transform infrared (FTIR) spectra were carried out using a Bruker spectrometer in the frequency range of 2000–600 cm^{-1} with a resolution of 4 cm^{-1}. The UV–vis diffuse reflectance spectra (DRS) of the samples were recorded in the range from 200 to 800 nm using a Hitachi U-3010 spectroscope equipped with an integrated sphere attachment, and $BaSO_4$ was used as a reference. The Brunauer–Emmett–Teller (BET) surface area was measured by Tristar II 3020. The nitrogen adsorption and desorption isotherms were measured at 77 K after degassing the samples. Electrochemical and photoelectrochemical measurements were performed in three-electrode quartz cells with a 0.1 M Na_2SO_4 electrolyte solution. Platinum wire was used as the counter electrode, and saturated calomel electrodes (SCE) were used as the reference electrodes, respectively. The as-prepared photocatalyst film electrodes on ITO served as the working electrode. The photoelectrochemical experiment results were recorded using an electrochemical system (CHI-660B, China). The intensity of light was 1 mW cm^{-2}. Potentials were given with reference to the SCE. The photoresponses of the photocatalysts as UV light on and off were measured at 0.0 V. Electrochemical impedance spectra (EIS) were measured at 0.0 V. A sinusoidal ac perturbation of 5 mV was applied to the electrode over the frequency range of 0.05–105 Hz. Moreover, the concentration of dye and their by-products were determined by HPLC (high performance liquid chromatography) using a Venusil XBP-C_{18} (3.9 × 200, Agela Technologies Inc.) column, Auto-sampler: 20 vials capacity with 6 line degasser channel, K-2501 ultraviolet absorbance detector. Two different kinds of solvents were prepared in this study. Solvent A was acetonitrile while solvent B was made from 0.1 M ammonium acetate and acetic acid (pH 5.3). The flow rate of the mobile phase was set at 0.8 ml min^{-1}. Before the analysis, the samples were filtered through Millipore discs of 0.45 μm to protect the chromatographic column.

2.4. Photodegradation experiment

The photocatalytic activities were evaluated by the decomposition of methylene blue (MB) under UV light (λ = 254 nm) and visible light irradiation (λ > 420 nm). The radial flux was measured by a power meter from the Institute of Electric Light Sources, Beijing. UV light was provided by an 11 W UV-light lamp (Institute of Electric Light Sources, Beijing) and the average light intensity was 0.91 mW cm^{-2}. Visible irradiation was obtained from a 500 W xenon lamp (Xujiang Electromechanical Plant, Nanjing, China) with a 420 nm cutoff filter. A certain amount of photocatalyst (50 mg for UV light, 25 mg for visible light) was totally dispersed in an aqueous solution of MB (100 ml, 0.01 mM for UV light, 50 ml, 0.01 mM for visible light). Before irradiation, the suspensions were magnetically stirred in the dark for 60 min to get absorption–desorption equilibrium between the photocatalyst and MB. At certain time intervals, 3 ml aliquots were sampled and centrifuged to remove the particles. The concentration of the MB was analyzed by a Hitachi U-3010 UV–vis spectrophotometer at 663 nm.

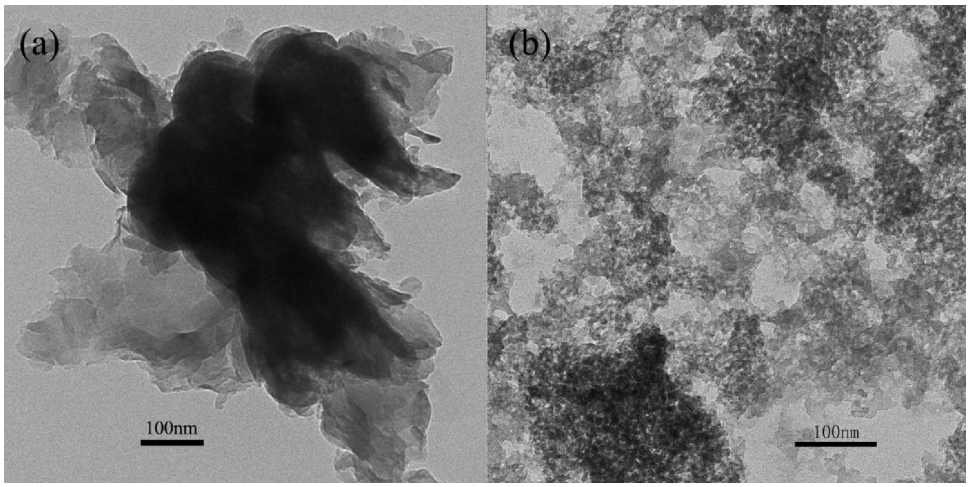

Fig. 1. TEM images of materials ((a) and (b)) mpg-C_3N_4 (c) ZnO.

3. Results and discussion

3.1. Structure and morphology of ZnO@mpg-C_3N_4

Fig. 1 shows transmission electron microscopy (TEM) images of bulk g-C_3N_4 and mpg-C_3N_4. As shown in Fig. 1a, most of irregular and larger plates are observed in the bulk-C_3N_4. While for mpg-C_3N_4, many spherical pores with a mean diameter of about 12 nm are observed to homogenously distribute on the plates of mpg-C_3N_4. These pores exactly reflect the geometric properties of the original template of SiO_2 particles, which have particle size of 12 nm. Compared with the bulk g-C_3N_4, the sheet layer becomes smaller and more fragmentary, which is due to the pores formation. So it can be deduced that the mpg-C_3N_4 might be more easily coated on the surface of ZnO which is helpful to form the core–shell structure of ZnO@mpg-C3N4. Additionally, due to many mesoporous formed in g-C_3N_4, the specific surface area of mpg-C_3N_4 (169.67 $m^2\ g^{-1}$) is greatly improved compared with bulk-C_3N_4 (7.45 $m^2\ g^{-1}$).

HRTEM is used to estimate C_3N_4 shell thickness and to show details of the coating structures. The HRTEM images of ZnO, ZnO@mpg-C_3N_4-4%, ZnO@mpg-C_3N_4-8% and ZnO@mpg-C_3N_4-20% are showed in Fig. 2a–d, respectively. As can be seen from the images, all the samples exhibit about the same interlayer spacing, about 0.26 nm, corresponding to (0 0 2) crystal planes of ZnO, indicating there is no change in the lattice structure of ZnO after surrounding by mpg-C_3N_4 shells. Fig. 2b shows that the thickness of mpg-C_3N_4 layer coated on the ZnO@mpg-C_3N_4-4% surface is about 0.437 nm, which is nearly close to the scale of monolayer C_3N_4 [22]. In the image of ZnO@mpg-C_3N_4-8%, the thickness of mpg-C_3N_4 shell is estimated to be 1.16 nm For ZnO@mpg-C_3N_4-20%, and it is increased to 4–6 nm. It can be seen that the thickness of the shell increases with the increase of the loading amount of mpg-C_3N_4, suggesting that it may be controlled by tuning the amount of mpg-C_3N_4 in the dispersion. The formation processes for the core–shell structure can be described by the two following steps: mpg-C_3N_4 is firstly exfoliated into sheet structures through an ultrasonic method in CH_3OH solvent, and then the mpg-C_3N_4 sheets will be spontaneously coated on the surface of ZnO to achieve a minimum surface energy. It should be pointed out that the thickness of mpg-C_3N_4 shell is not nonuniform and not in proportion to the amount of mpg-C_3N_4 dispersed in solution. This phenomenon is generated due to the different controlling factors. At the beginning, the step of mpg-C_3N_4 coating on the surface of ZnO is mainly a thermodynamic process. With the thickness of mpg-C_3N_4 shell further increasing, thermodynamic factor does not play a major role and kinetic factor is becoming the decisive factor. Consequently, the thickness of the coating layer is not controlled by their surface energy, but might be controlled by other factors, such as, the dispersion of ZnO particles and mpg-C_3N_4 in solution at that time, making a nonuniform thickness of mpg-C_3N_4 shell.

To identify the phase structures, the wide-spectra (20.0–70.0°) and narrow-spectra (26.0–29.0°) XRD patterns of ZnO, mpg-C_3N_4 and the ZnO@mpg-C_3N_4 samples with the different mpg-C_3N_4 loading amount are shown in Fig. S1 and Fig. 3, respectively. Fig. S1 shows that the crystal phase of ZnO do not change after having been covered by the mpg-C_3N_4 and its diffraction peaks are in good agreement with the hexagonal wurtzite crystal phase of ZnO (JCPDS 65-3411). The mpg-C_3N_4 sample has a characteristic peak at 27.4°, which can be indexed as the (0 0 2) diffraction plane. However, this peak cannot be clearly observed in the wide-spectra XRD patterns of all ZnO@mpg-C_3N_4 samples. This phenomenon might be that the relative intensities of ZnO peaks are too much strong to show the peak of mpg-C_3N_4. In order to clearly observe the peaks of mpg-C_3N_4 in ZnO@mpg-C_3N_4 samples, the narrow-spectra XRD patterns in the region of 2θ (26.0–29.0°) are given in Fig. 3. The characteristic peak of crystalline mpg-C_3N_4 cannot be observed at the low loading amount of mpg-C_3N_4 (1% and 2%). When the loading amount of mpg-C_3N_4 is more than 3%, a weak peak at 27.4° appears. As the loading amount of mpg-C_3N_4 further increasing, the intensity of this peak remarkably improves. Fig. S1 and Fig. 3 also indicate that the mpg-C_3N_4 coated on the surface of ZnO exhibits a short-range order due to the small sheet layers of mpg-C_3N_4.

The FT-IR spectra of ZnO, mpg-C_3N_4, and a series of ZnO@mpg-C_3N_4 photocatalysts is shown in the Supporting Information (Fig. S2). In the FT-IR spectrum of C_3N_4, the peak at 1637 cm^{-1} is attributable to the C=N stretching vibration modes, while the peaks at 1243 cm^{-1}, 1320 cm^{-1} and 1403 cm^{-1} are due to the aromatic C–N stretching [23–25]. The peak at 808 cm^{-1} is related to the *s*-triazine ring modes [24]. In the FT-IR spectrums of the ZnO@mpg-C_3N_4 photocatalysts, the main characteristic peaks of both C_3N_4 and ZnO are observed, indicating that the mpg-C_3N_4 has been coated on the surface of the ZnO. Furthermore, with the increase of the mass ratio of the mpg-C_3N_4 to ZnO, the intensity of the characteristic peak of C_3N_4 in the ZnO@ mpg-C_3N_4 samples increases.

The UV–vis diffuse reflection spectra of ZnO and ZnO@mpg-C_3N_4 photocatalysts with different mpg-C_3N_4 mass ratios are shown in Fig. 4. As expected, a sharp absorption edge rises at 400 nm for ZnO. The fundamental absorption edge of the mpg-C_3N_4 occurs at ca. 570 nm, which exhibits a band gap considered to be 2.7 eV. Meanwhile, the ZnO@mpg-C_3N_4 photocatalysts show the same absorbance edge with ZnO, but extend the absorbance to the

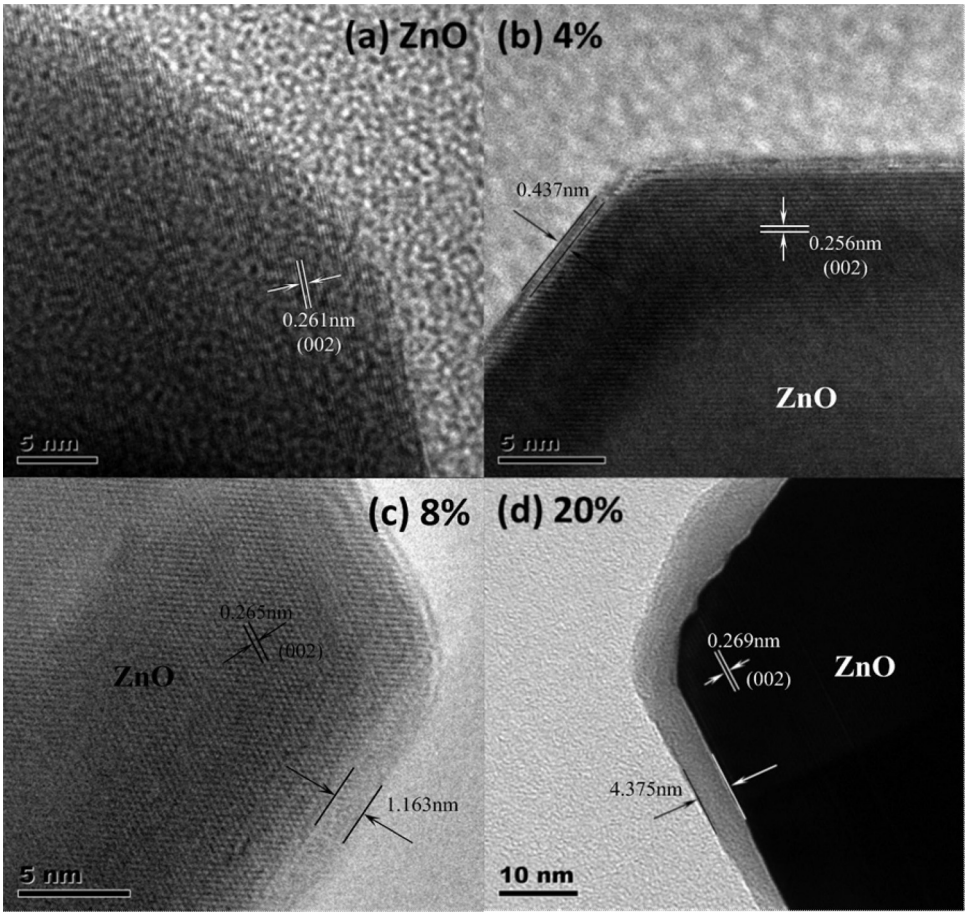

Fig. 2. HRTEM images of (a) ZnO, (b) ZnO@mpg-C_3N_4-4%, (c) ZnO@mpg-C_3N_4-8%, (d) ZnO@mpg-C_3N_4-20%.

visible region due to the presence of mpg-C_3N_4 on the ZnO surface. The fact that the absorption edges of all the ZnO@mpg-C_3N_4 samples remain the same with ZnO indicates that coating mpg-C_3N_4 on the ZnO surface does not change the band gap energies of ZnO. While the absorption intensity of the ZnO@mpg-C_3N_4 samples in the visible region increases with the increase of the loading amounts of mpg-C_3N_4.

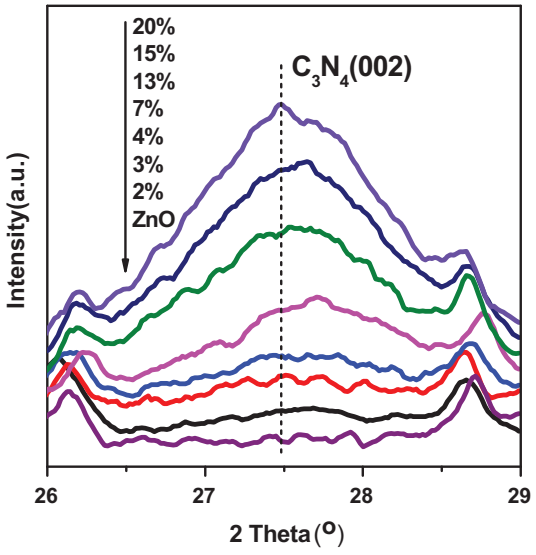

Fig. 3. The magnified XRD patterns of ZnO and ZnO@mpg-C_3N_4 photocatalysts.

3.2. Photocatalytic activity and photocurrent

The photocatalytic activities of the ZnO@mpg-C_3N_4 samples were evaluated by degradation of methylene blue (MB) in solution under the UV light and visible light irradiation, which are shown in Fig. 5a and b, respectively. The photocatalytic degradation of organic pollutants generally follows pesudo-first-order kinetics. As shown in Fig. 5a, all of the ZnO@mpg-C_3N_4 photocatalysts exhibited higher photocatalytic activity than the pristine ZnO sample under UV light irradiation. The photocatalytic activity of ZnO@mpg-C_3N_4

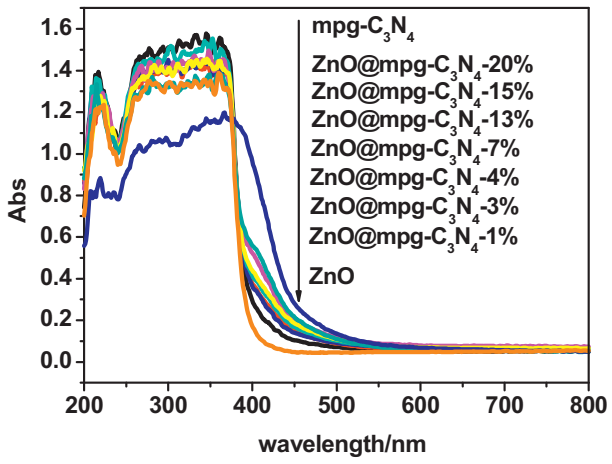

Fig. 4. UV–vis diffuse reflection spectra of ZnO, mpg-C_3N_4 and ZnO@mpg-C_3N_4 photocatalysts.

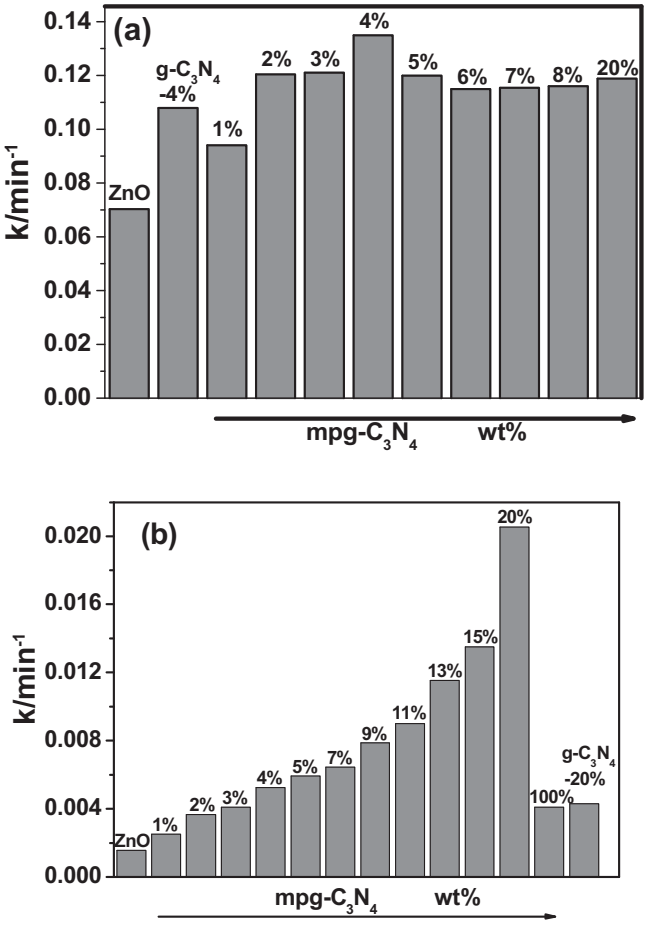

Fig. 5. Apparent rate constants for the photocatalytic degradation of MB over ZnO, ZnO@g-C_3N_4 and ZnO@mpg-C_3N_4 photocatalysts (a) under UV light irradiation (λ = 254 nm) and (b) under visible light irradiation (λ > 420 nm).

increases gradually with the increase of the loading amount of mpg-C_3N_4 and reaches the optimum activity when the loading amount of mpg-C_3N_4 reaches to 4 wt% (ZnO@mpg-C_3N_4-4%). The apparent rate constant of ZnO@mpg-C_3N_4-4% is 0.135 min^{-1}, which is about 2.0 times as high as that of ZnO (k = 0.070 min^{-1}). However, as the loading amount of mpg-C_3N_4 further increases, the degradation rate gradually decreases, and finally remains unchanged. This change in UV activity of ZnO@mpg-C_3N_4 samples may be attributed to the high efficiency of charge separation induced by the hybrid effect of mpg-C_3N_4 and ZnO. At the low mpg-C_3N_4 loading, especially when the cover thickness of C_3N_4 is approximately monolayer structure, the C_3N_4 shells are beneficial for charge transfer at ZnO interfaces. However, at the same time, the C_3N_4 shells will shield UV light off ZnO, which lead to decreasing the photocatalytic activity. Therefore, due to the demands of both the charge transfer and light absorption, the photocatalytic activity of ZnO@mpg-C_3N_4 samples first increases and then decreases with the increasing thickness of mpg-C_3N_4. From Fig. 5a, it can be seen that ZnO@mpg-C_3N_4-4% (k = 0.135 min^{-1}) has a higher photocatalytic activity than that of ZnO@g-C_3N_4-4% (k = 0.108 min^{-1}), suggesting that coating mpg-C_3N_4 on the surface of ZnO has a better effect on improving the photocatalytic activity than bulk C_3N_4. This fact can be explained by the following reasons. One might be that the mesoporous existed in C_3N_4 can be regarded as the channels, through which UV light can easily pass and then excite ZnO. Another is that mpg-C_3N_4 facilitates the formation of core–shell structure induced by the lattice match, which is supposed to favor the transport of both electrons and holes across the photocatalyst. Finally, the large specific surface area of mpg-C_3N_4 can improve the contact chance between dye and photocatalyst, which can accelerate the rate of the photocatalytic reaction.

Fig. 5b shows the MB photodegradation rate constants on ZnO, mpg-C_3N_4 and a series of ZnO@mpg-C_3N_4 photocatalysts under visible light irradiation. The ZnO@mpg-C_3N_4 photocatalysts exhibit excellent photocatalytic activity under visible light irradiation (λ > 420 nm). Different from the UV activity, the visible light photocatalytic activity is enhanced gradually with the loading amount of mpg-C_3N_4 increasing. The reason is that the visible activities for ZnO@mpg-C_3N_4 samples are due to the excitation of C_3N_4. Increasing the thickness of mpg-C_3N_4 shell will not only enhance the visible light absorption, but also benefit for charge transfer at the heterojunction interfaces. Furthermore, the core–shell structure induced by the lattice match will not only promotes the charge transfer at the heterojunction interfaces, but also suppress the aggregation of the C_3N_4 particles [26] and thus increase the surface area of mpg-C_3N_4. So the activity order for ZnO@mpg-C_3N_4 samples under visible light is different from that under UV light. Except the ZnO@mpg-C_3N_4-1% and ZnO@mpg-C_3N_4-2% samples, all the ZnO@mpg-C_3N_4 photocatalysts exhibit the higher photocatalytic activity than the mpg-C_3N_4 sample. The apparent rate constant of ZnO@mpg-C_3N_4-20% is 0.0205 min^{-1}, which is 5.0 times higher than that of mpg-C_3N_4 (k = 0.00408 min^{-1}). In addition, the photocatalytic activity of ZnO@mpg-C_3N_4 increases gradually with an increasing the loading amount of mpg-C_3N_4. It should note that ZnO@mpg-C_3N_4 (k = 0.0205 min^{-1}) has the higher photocatalytic activity than ZnO@g-C_3N_4-20% (k = 0.00428 min^{-1}). The reason is that the larger surface area and porous structure of mpg-C_3N_4 can not only increase the absorption of dye onto ZnO@g-C_3N_4 photocatalyst, but also is conductive to the electrons transfer, resulting in the higher photocatalytic activity of ZnO@mpg-C3N4.

The transient photocurrent responses of a photocatalysis may directly correlate with the recombination efficiency of the photogenerated carriers [27–29]. Fig. 6a and b, shows the transient photocurrent responses of ZnO, mpg-C_3N_4, ZnO@g-C_3N_4 and ZnO@mpg-C_3N_4 electrodes under UV and visible light irradiation, respectively. A generation of photocurrent with good reproducibility for all samples is observed via four on-off cycles. This indicates that the electrode is stable and the photocurrent is quite reversible. The photocurrent of the optimum ZnO@mpg-C_3N_4 sample electrode under UV light irradiation (Fig. 6a) is about 1.7 times as high as that of the pristine ZnO, while it is about 3.3 times as high as that of the mpg-C_3N_4 electrode under visible light irradiation (Fig. 6b). The photocurrent enhancement of the ZnO@mpg-C_3N_4 photocatalyst indicates an enhanced photoinduced electrons and holes separation, which could be attributed to the match of lattice and energy level between the mpg-C_3N_4 shell and the ZnO core. The photocurrent of ZnO@mpg-C_3N_4-4% is higher than that of ZnO@mpg-C_3N_4-20% under UV light irradiation, while the inverse result is obtained under visible light irradiation. This reason is ascribed to the different excited semiconductor (ZnO or mpg-C_3N_4) and the different path of the separation and transportation of electron–hole pairs under UV light and the visible light irradiation, which will be discussed below.

3.3. *Mechanism of photocatalytic activity enhancement*

To reveal the photocatalytic process, the HPLC chromatograms of MB photodegradation by ZnO, mpg-C_3N_4 and ZnO@mpg-C_3N_4 photocatalysts under UV and visible light irradiation are shown in Fig. 7a and b, respectively. In Fig. 7a, two peaks at 4.6 and 4.2 min are detected from the chromatogram spectra of the original reaction solution. The peak at 4.6 min is attributed to the initial MB. Another peak at 4.2 min is attributed to the azure B due to the self-degradation of MB [30]. Under UV light irradiation, two new

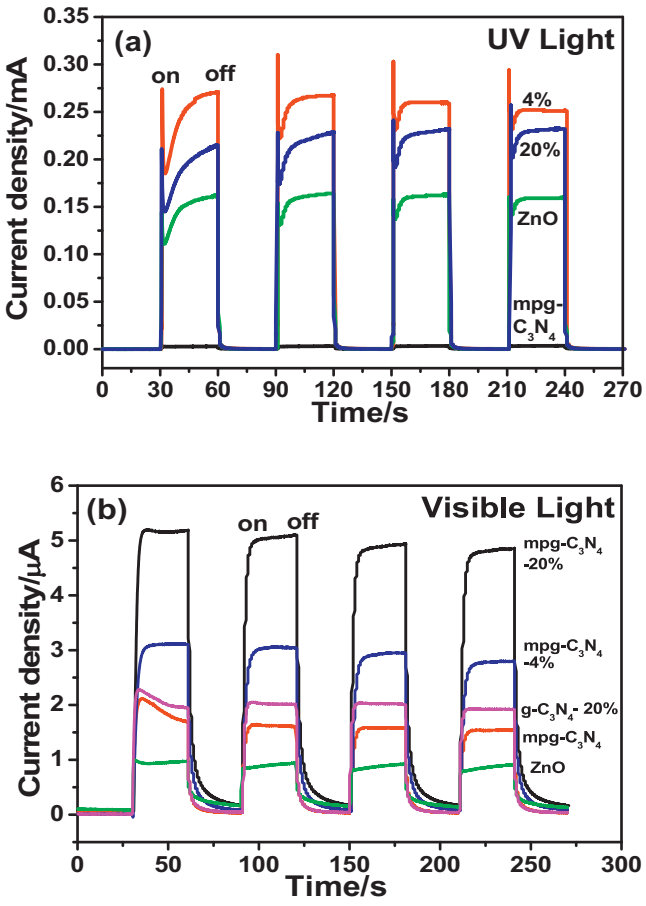

Fig. 6. The transient photocurrent density responses of ZnO, mpg-C_3N_4, ZnO@g-C_3N_4 and ZnO@mpg-C_3N_4 photocatalysts electrodes with light on/off cycles: (a) under UV light irradiation ($\lambda = 254$ nm) and (b) under visible light irradiation ($\lambda > 420$ nm). [Na_2SO_4] = 0.1 M.

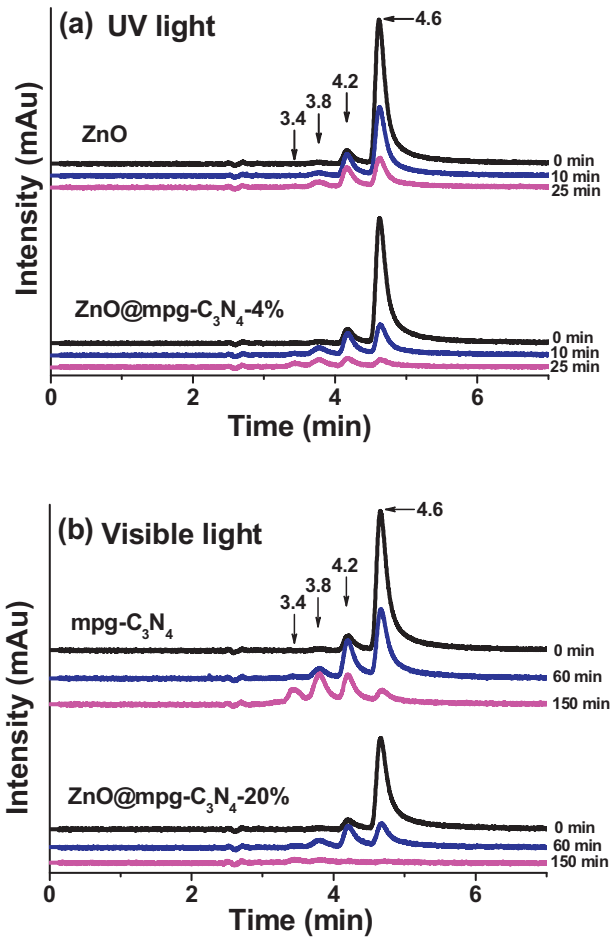

Fig. 7. HPLC Chromatogram of MB photodegradation by (a) ZnO and ZnO@mpg-C_3N_4-4% under UV light irradiation ($\lambda = 254$ nm), and (b) mpg-C_3N_4 and ZnO@mpg-C_3N_4-20% under visible light irradiation ($\lambda > 420$ nm).

peaks located at 3.8 and 3.4 min appear, indicating the formation of the intermediate products during the MB photodegradation process. Additionally, the characteristic peak of MB at 4.6 nm decreases gradually with the increase of the degradation time, while those peaks for the intermediate products increases firstly and then decrease, indicating that MB molecular is gradually degraded to CO_2 and H_2O through the photocatalytic degradation of intermediate products [31,32]. After 25 min of the photocatalytic degradation, the peak intensity of MB by ZnO@mpg-C_3N_4-4% degradation is lower than that by ZnO degradation, confirming that ZnO@mpg-C_3N_4-4% has a higher UV light photocatalytic activity than ZnO. However, the same intermediate products were obtained by both ZnO@mpg-C_3N_4-4% and ZnO photodegradation. This fact indicates that both them have the same oxidation mechanism for MB degradation under UV light. Fig. 7b gives the photodegradation of MB by mpg-C_3N_4 and ZnO@mpg-C_3N_4 photocatalysts under visible light irradiation from 0 to 150 min. The same peaks of the intermediate products are observed in the HPLC chromatograms of MB photodegradation under the visible light. This phenomenon also suggests that the degradation mechanisms of mpg-C_3N_4 and ZnO@mpg-C_3N_4 are identical under visible light and the degradation process has not changed after mpg-C_3N_4 coating on the surface of ZnO. Furthermore, it can be seen that the MB can be completely degraded by ZnO@mpg-C_3N_4 within 150 min under visible light irradiation, showing that ZnO@mpg-C_3N_4 not only exhibits a good photocatalytic activity under UV light, but also is an effective photocatalyst under visible light.

It is well known that the photocatalytic activity is mainly governed by phase structure, adsorption ability, and separation efficiency of photogenerated electrons and holes [33,34]. As can be seen from the XRD spectra, the crystal phase structure of ZnO does not changed after coating the mpg-C_3N_4. The BET surface area of ZnO is 9.65 $m^2\ g^{-1}$ and that of ZnO@mpg-C_3N_4-4% is 13.16 $m^2\ g^{-1}$, showing that coating the mpg-C_3N_4 has a little increase in BET surface area of ZnO. An adsorption experiment was performed to evaluate the adsorption ability of the ZnO and ZnO@mpg-C_3N_4-4% photocatalysts (supporting information Fig. S3). After equilibration in the dark for 30 min, 7% and 17% of MB was absorbed by the pristine ZnO and ZnO@mpg-C_3N_4-4% photocatalysts, respectively. The enhancement of adsorption could be contributed not only to the increase of BET surface area of ZnO, but also to the π–π stacking between MB and C_3N_4 [33]. The MB adsorption improvement is a good supplement for the high photocatalytic activity of the ZnO@mpg-C_3N_4-4% photocatalysts.

The limited adsorption enhancement is not the major factor of the significant improvement of the photocatalytic activity of ZnO. The important reason is due to the effective separation of the photogenerated electron–hole pairs induced by the energy level match between C_3N_4 and ZnO. The interface charge separation efficiency can be investigated by the typical electrochemical impedance spectra (presented as Nyquist plots). Fig. 8a and b show the EIS Nynquist plots of ZnO, mpg-C_3N_4, ZnO@g-C_3N_4 and ZnO@mpg-C_3N_4 photocatalysts before and after light irradiation under UV and visible light irradiation, respectively. The radius of

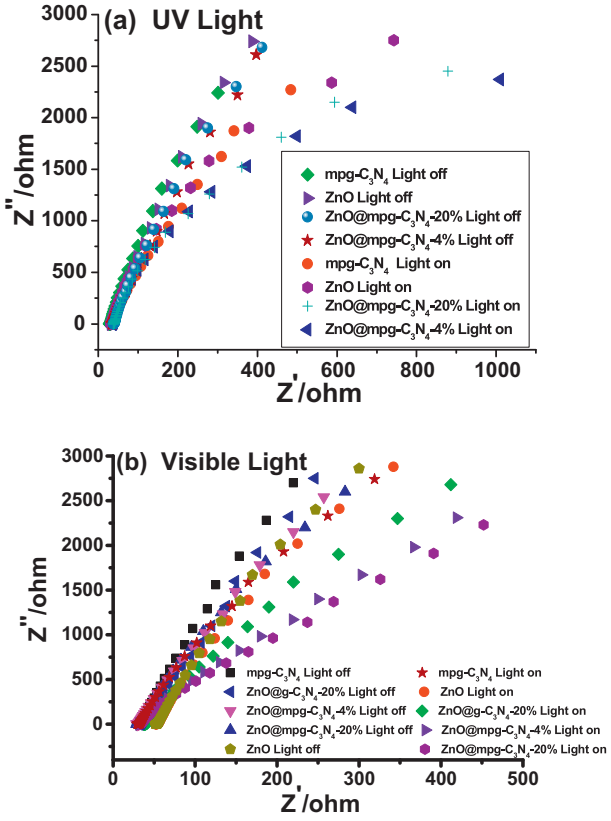

Fig. 8. Nyquist plots for ZnO, mpg-C_3N_4 and ZnO@mpg-C_3N_4-4%, ZnO@mpg-C_3N_4-20%, ZnO@g-C_3N_4-20% in aqueous solution (a) in the dark and under UV light illumination and (b) in the dark and under visible light illumination [Na_2SO_4 = 0.1 M].

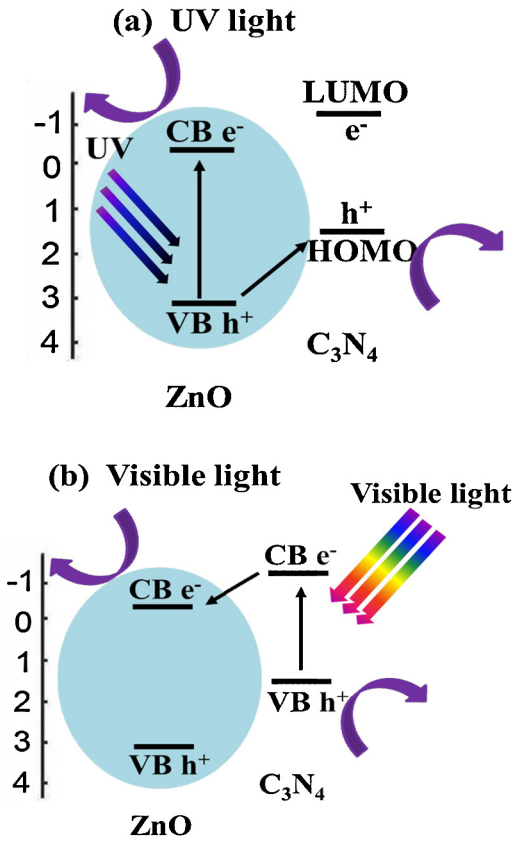

Fig. 9. Schematic drawing illustrating the mechanism of charge separation and photocatalytic activity of the ZnO@mpg-C_3N_4 photocatalyst (a) under UV light irradiation (λ = 254 nm) and (b) under visible light irradiation (λ > 420 nm).

the arc on the EIS spectra reflects the interface layer resistance occurring at the surface of electrode. This smaller arc radius implies the higher efficiency of charge transfer [28]. Fig. 8 shows that the diameters of the arc radius for the ZnO@mpg-C_3N_4-4% and ZnO@mpg-C_3N_4-20% electrode are smaller than that for the ZnO or mpg-C_3N_4 electrode, in the cases of UV or visible light irradiation, demonstrating that the coating mpg-C_3N_4 onto the surface of ZnO can dramatically enhance the separation and transfer efficiency of the photogenerated electron–hole pairs through an interfacial interaction between mpg-C_3N_4 and ZnO. It can be observed that the radius of ZnO@mpg-C_3N_4-4% is smaller than that of ZnO@mpg-C_3N_4-20% under UV light, while the inverse result is obtained under visible light irradiation. This result is agreement with the transient photocurrent responses of these photocatalyst.

A scheme for the separation and transportation of electron–hole pairs at the interface of ZnO@mpg-C_3N_4 photocatalysts under UV and visible light is proposed in Fig. 9a and b, respectively. As can be seen in Fig. 9a, ZnO can absorb UV light to produce the photogenerated electron–hole pairs. Since the valence band (VB) position of ZnO is lower than the highest occupied molecular orbital (HOMO) orbit of C_3N_4, [22,35] the photogenerated holes on ZnO could easily transfer to mpg-C_3N_4, making charge separation more efficient and reducing the probability of recombination, leading to an enhanced photocatalytic activity of ZnO@mpg-C_3N_4 under the UV light irradiation. Fig. 7b gives a possible schematic mechanism of the visible light activity. ZnO itself cannot be excited under visible light irradiation. When C_3N_4 absorbs the visible light, it can induce π–π^* transition and transport the excited-state electrons from the VB to the CB. The CB potential of C_3N_4 (−1.12 eV) [22] is more negative than the CB edge of ZnO (−0.5 eV) [14], so the excited electron on C_3N_4 could directly inject into the CB of ZnO. These electrons would subsequently transfer to the surface of photocatalyst to react with oxygen to form superoxide and hydroxyl radicals. The radicals are able to oxidize the pollutant due to their high oxidative capacity, thus dramatically producing visible light photocatalytic activity. Therefore, the hybrid effect and energy level match between two semiconductors are two key factors for the effective separation of photogenerated electron–hole pairs. On the other hand, the core–shell structure of ZnO@mpg-C_3N_4 is supposed to favor the transport of both electrons across individual ZnO particle driven by strong dipolar fields arising from charged surface domains. These charged surface domains of ZnO would, in effect, electrostatically drive the photoexcited electrons or holes from the core solids into the conduction and valence bands of shells.

4. Conclusion

ZnO@mpg-C_3N_4 core–shell photocatalysts was successfully synthesized via a facile ultrasonic dispersion method. After introduction of mpg-C_3N_4, both the UV light and the visible light photocatalytic activity of ZnO were significantly increased. The UV activity of ZnO can be increased by 2.0 times due to the surface hybridization by the mpg-C_3N_4. The enhancement in photocatalytic performance under the visible light irradiation is ascribed to the high separation and easy transfer of photogenerated electron–hole pairs at the heterojunction interfaces derived from the match of lattice and energy level between the mpg-C_3N_4 shell and ZnO core.

Acknowledgement

This present work is supported by the National Natural Science Foundations of China (Grant No. 21106138), the Fundamental Research Funds for the Central Universities (Grant

No. 2011YXL062), Open fund of National Laboratory of Mineral Materials (Grant No. 09A003). Natural Science Foundation of Tianjin (No. 12JCQNJC06000). Daimei Chen and Kewei Wang contributed equally to this work.

Appendix A. Supplementary data

Supplementary data associated with this article can be found, in the online version, at http://dx.doi.org/10.1016/j.apcatb.2013.09.039.

References

[1] S.N. Frank, A.J. Bard, J. Am. Chem. Soc. 99 (1977) 303–304.
[2] T.L. Thompson, J.T. Yates, Chem. Rev. 106 (2006) 4428–4453.
[3] A. Mills, S. Le Hunte, J. Photochem. Photobiol. A: Chem. 108 (1997) 1–35.
[4] K. Ayoub, E.D. van Hullebusch, M. Cassir, A. Bermond, J. Hazard. Mater. 178 (2010) 10–28.
[5] U.G. Akpan, B.H. Hameed, J. Hazard. Mater. 170 (2009) 520–529.
[6] H. Zhang, G. Chen, D.W. Bahnemann, J. Mater. Chem. 19 (2009) 5089–5121.
[7] A.Z. Moshfegh, J. Phys. D: Appl. Phys. 42 (2009) 233001.
[8] H. Qin, W. Li, Y. Xia, T. He, ACS Appl. Mater. Interfaces 3 (2011) 3152–3156.
[9] X. Qiu, L. Li, J. Zheng, J. Liu, X. Sun, G. Li, J. Phys. Chem. C: Nanomater. Interfaces 112 (2008) 12242–12248.
[10] W. Lu, S. Gao, J. Wang, J. Phys. Chem. C: Nanomater. Interfaces 112 (2008) 16792–16800.
[11] J. Liqiang, W. Baiqi, X. Baifu, L. Shudan, S. Keying, C. Weimin, F. Honggang, J. Solid State Chem. 177 (2004) 4221–4227.
[12] M. Zhang, T. An, X. Hu, C. Wang, G. Sheng, J. Fu, Appl. Catal. A: Gen. 260 (2004) 215–222.
[13] R.S. Mane, W.J. Lee, H.M. Pathan, S.-H. Han, J. Phys. Chem. B 109 (2005) 24254–24259.
[14] H. Fu, T. Xu, S. Zhu, Y. Zhu, Environ. Sci. Technol. 42 (2008) 8064–8069.
[15] H. Zhang, Y. Zhu, J. Phys. Chem. C 114 (2010) 5822–5826.
[16] Y. Wang, R. Shi, J. Lin, Y. Zhu, Energy Environ. Sci. 4 (2011) 2922–2929.
[17] X. Wang, K. Maeda, A. Thomas, K. Takanabe, G. Xin, J.M. Carlsson, K. Domen, M. Antonietti, Nat. Mater. 8 (2009) 76–80.
[18] X. Wang, K. Maeda, X. Chen, K. Takanabe, K. Domen, Y. Hou, X. Fu, M. Antonietti, J. Am. Chem. Soc. 131 (2009) 1680–1681.
[19] C. Pan, J. Xu, Y. Wang, D. Li, Y. Zhu, Adv. Funct. Mater. 22 (2012) 1518–1524.
[20] Y. Wang, X. Bai, C. Pan, J. He, Y. Zhu, J. Mater. Chem. 22 (2012) 11568–11573.
[21] F. Goettmann, A. Fischer, M. Antonietti, A. Thomas, Angew. Chem. Int. Ed. 45 (2006) 4467–4471.
[22] S.C. Yan, S.B. Lv, Z.S. Li, Z.G. Zou, Dalton Trans. 39 (2010) 1488–1491.
[23] Y.C. Zhao, D.L. Yu, H.W. Zhou, Y.J. Tian, O. Yanagisawa, J. Mater. Sci. 40 (2005) 2645–2647.
[24] X. Li, J. Zhang, L. Shen, Y. Ma, W. Lei, Q. Cui, G. Zou, Appl. Phys. A 94 (2009) 387–392.
[25] L. Liu, D. Ma, H. Zheng, X. Li, M. Cheng, X. Bao, Microporous Mesoporous Mater. 110 (2008) 216–222.
[26] X. Chen, Y.-S. Jun, K. Takanabe, K. Maeda, K. Domen, X. Fu, M. Antonietti, X. Wang, Chem. Mater. 21 (2009) 4093–4095.
[27] H. Liu, S. Cheng, M. Wu, H. Wu, J. Zhang, W. Li, C. Cao, J. Phys. Chem. A 104 (2000) 7016–7020.
[28] W.H. Leng, Z. Zhang, J.Q. Zhang, C.N. Cao, J. Phys. Chem. B 109 (2005) 15008–15023.
[29] H. Park, W. Choi, J. Phys. Chem. B 107 (2003) 3885–3890.
[30] M.A. Rauf, M.A. Meetani, A. Khaleel, A. Ahmed, Chem. Eng. J. 157 (2010) 373–378.
[31] C. Yogi, K. Kojima, N. Wada, H. Tokumoto, T. Takai, T. Mizoguchi, H. Tamiaki, Thin Solid Films 516 (2008) 5881–5884.
[32] A. Orendorz, C. Ziegler, H. Gnaser, Appl. Surf. Sci. 255 (2008) 1011–1014.
[33] H. Zhang, X. Lv, Y. Li, Y. Wang, J. Li, ACS Nano 4 (2009) 380–386.
[34] L.-W. Zhang, H.-B. Fu, Y.-F. Zhu, Adv. Funct. Mater. 18 (2008) 2180–2189.
[35] A. Hagfeldt, M. Graetzel, Chem. Rev. 95 (1995) 49–68.